ANNALS OF GEOPHYSICS, 62, 4, GM454, 2019; doi: 10.4401/ag-7780

"THE RESPONSE OF HIGH LATITUDE IONOSPHERE TO THE 2015 JUNE 22 STORM"

Giulia D'Angelo[*,1], Mirko Piersanti[2,3], Lucilla Alfonsi[4], Luca Spogli[4,5], Igino Coco[4], Guozhu Li[6] and Ning Baiqi[6]

(1) Dipartimento di Matematica e Fisica, Università degli Studi "Roma Tre", Rome, Italy
(2) Istituto di Astrofisica e Planetologia Spaziali, Rome, Italy
(3) Consorzio Area di Ricerca in Astrogeofisica, Università di L'Aquila, L`Aquila, Italy
(4) Istituto Nazionale di Geofisica e Vulcanologia, Rome, Italy
(5) SpacEarth Technology, Via di Vigna Murata 605, 00143, Rome, Italy
(6) Institute of Geology and Geophysics, Chinese Academy of Sciences, Beijing, 100029, China

Article history
Receveid **May 29, 2018**; accepted **December 4, 2018.**
Subject classification:
High-latitude Ionosphere; Geomagnetic storm, Magnetosphere-Ionosphere coupling; GNSS scintillation; Space Weather

ABSTRACT

This work investigates physical mechanisms triggering phase scintillations on L–band signals under strong stormy conditions. Thanks to selected ground–based Global Navigation Satellite Systems (GNSS) receivers, located both in Antarctica and in the Arctic, an inter–hemispheric comparison between high latitude ionospheric observations in response to the peculiar solar wind conditions occurred on June 22, 2015 is here shown. To trace back the observed phase scintillations to the physical mechanisms driving it, we combine meas–urements from GNSS receivers with *in-situ* and ground–based observations. Our study highlights the ionospheric scenario in which ir–regularities causing scintillation form and move, leveraging on a multi–observation approach. Such approach allows deducing that scintillations are caused by the presence of fast–moving electron density gradients originated by particle precipitation induced by solar wind variations. In addition, we show how the numerous and fast oscillations of the North–South component of the interplanetary mag–netic field ($B_{z,\,IMF}$) result to be less effective in producing moderate/intense scintillation events than during period of long lasting nega–tive values. Finally, we also demonstrate how the *in-situ* electron density data can be used to reconstruct the evolution of the ionospheric dynamics, both locally and globally.

1. INTRODUCTION

The geomagnetic storm occurred from 21 to 24 June 2015 is one of the largest geomagnetic storms of the 24th solar cycle. Beside its intensity, the peculiarity of the storm lies in its occurrence during the summer solstice and in resulting from the superposition of several solar events. In fact, it was caused by a series of three inter–planetary shocks hitting the Earth's magnetosphere at 16:45 UT on June 21, at 05:45 UT on June 22 and at 18:30 UT on June 22, 2015, respectively. Unlike the 2015 St. Patrick's storm that was caused by multiple Inter–planetary Coronal Mass Ejections (ICMEs), all the June shocks resulted from single ejecta (Liu et al., 2015). Fig–ure 1 reports, from top to bottom, the Interplanetary Magnetic Field (IMF) amplitude $|B|_{IMF}$, the X component ($B_{x,\,IMF}$), Y component ($B_{y,\,IMF}$), Z component ($B_{z,\,IMF}$), the solar wind (SW) density, the SW proton temperature, the SW velocity, the SW dynamic pressure P, the *SYM-H* index and the AU (black) and AL (red) indices from 21

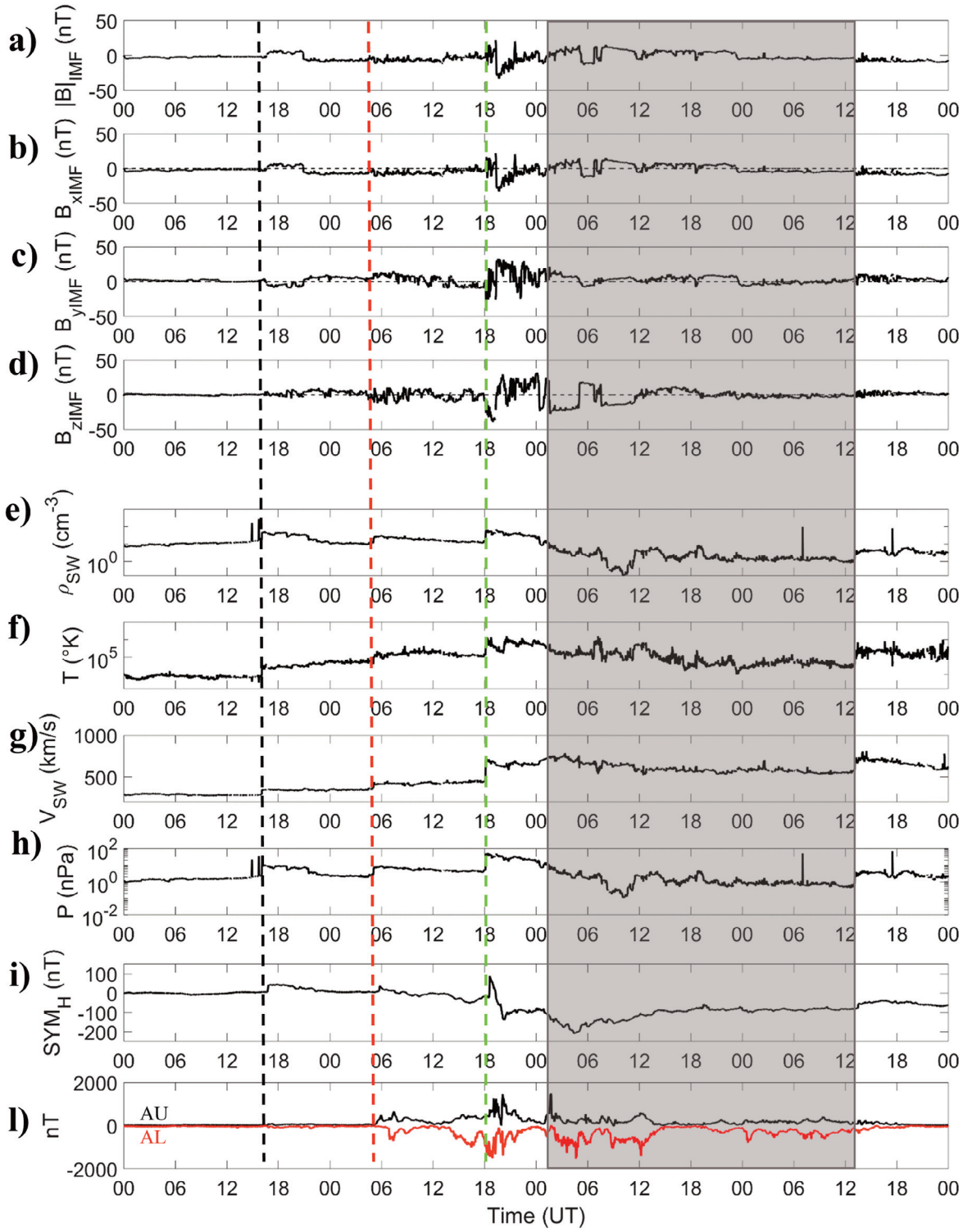

FIGURE 1. The solar wind (SW) observations (WIND spacecraft) and the geomagnetic response at low and high latitudes on June 21–24, 2015. From the top to the bottom: (a) $|B|_{IMF}$; (b) $B_{x,\,IMF}$; (c) $B_{y,\,IMF}$; (d) $B_{z,\,IMF}$; (e) the SW density ρ_{SW}; (f) the SW proton temperature T_{SW}; (g) the SW velocity V_{SW}; (h) the SW dynamic pressure P; (i) the *SYM-H* index; (l) the AU (black line) and the AL (red line) indices. The shaded region indicate the ICME interval and the dashed vertical lines mark the three shocks arrival at WIND (black the first, red the second, green the third, respectively).

to 24 June 2015. The shaded region indicate the ICME interval and the dashed vertical lines mark the corre–sponding shocks arrivals at WIND.

As reported by several authors [see e.g. Astafyeva et al., 2017; Piersanti et al., 2017; Cherniak and Za–kharenkova, 2017] and shown in Figure 1, the first

shock (black dashed line), accompanied by sharp changes in the SW density (panel e), temperature (panel f) and speed (panel g), compressed the Earth's magnetosphere and caused a sudden increase of the *SYM-H* of ~40 nT (panel i). Anyway, since the North–South component ($B_{z, IMF}$) of the IMF remained at most positive at the shock arrival (panel d), no substorm activity follows (panel l).

The second shock (red dashed line) was accompanied by a small solar wind density increase (panel e), causing an enhancement in the *SYM-H* of ~20 nT (panel i). At the shock's arrival, the $B_{z, IMF}$ turned negative (panel d) causing a sharp enhancement of the auroral activity, as visible in panel l. Then, $B_{z, IMF}$ fluctuated around zero until the arrival of the third shock (panel d) and a smaller decrease in the *SYM-H* index was observed (~ –40 nT, panel i). The last shock (green dashed line), accompanied by a large and sudden increase in solar wind and IMF components, caused a large and sudden increase in the *SYM-H* index up to ~88 nT at 18:37 UT (e.g., storm sudden commencement, panel i). The ejecta following this shock was characterized by a large negative $B_{z, IMF}$ (–39 nT, panel d), that caused a drop of the *SYM-H* index to –208 nT (on June 23, panel i) and, consequently, a strong auroral activity (panel l). Such conditions led to unusual responses of the ionosphere–thermosphere system labelled by both inter–hemispheric asymmetries and latitudinal differences.

The multi–instrumental works by Prikryl and co–authors [2011, 2013 and 2015] on the interhemispheric response to geospace forcing highlighted how the main asymmetries are due to the IMF dawn–dusk component, being responsible of the cusp location, and of the main orientation of the plasma convection within the polar cap. The combination of both effects results into a different occurrence of plasma patches between the two hemispheres, so leading to causing significant differences in the scintillation patterns over high–Arctic regions and over Antarctica. However, the solstice conditions, under which the June 2015 storm occurred, make the explanation of the inter–hemispheric asymmetry and latitudinal development very challenging, as reported in the recent literature [Astafyeva et al., 2016; Mansilla, 2017; Cherniak and Zakharenkova, 2017]. In fact, Mansilla [2017], which performed a global study of the ionospheric Total Electron Content (TEC) from high to low latitudes, observed asymmetries of the TEC response in both hemispheres. More in detail, he observed a TEC increase in the Southern hemisphere well correlating with an increase of the O/N_2 ratio. Correspondingly, he observed a decrease in the Northern hemisphere, not associated with a decrease in O/N_2 ratio. In addition, Astafyeva et al. [2016], who analysed variations of the ionospheric vertical TEC and electron density in the topside ionosphere during the initial and the main phases of the storm, observed a pronounced hemispheric asymmetry in the nigh time topside ionosphere. Specifically, in the Northern Hemisphere (summer), they observed an extreme enhancement in the investigated parameters attributed to the combination among the prompt penetration electric fields, the disturbance dynamo and the storm–time thermospheric circulation. Cherniak and Zakharenkova [2017], investigating the ionospheric irregularities through a chain of Global Navigation Satellite System (GNSS) located in both hemispheres from middle to high latitudes, found a good correlation between the occurrence of ionospheric irregularities and the variations of the AE and the *SYM-H* indices.

To provide further insights about the physical mechanisms leading to the irregularities formation and their effect on GNSS satellites, our study focuses on the scintillation events occurred in the high latitude regions of both hemispheres on June 22, when the bulk of the storm–driven ionospheric disturbances are observed. In particular, we analyse scintillation events recorded by five stations distributed both in the Arctic and in Antarctica. To trace back the observed scintillations to the physical background triggering the irregular ionosphere, we combine the information coming from TEC and from scintillation indices with the observations obtained from *in-situ* data (Swarm and Polar–orbiting Operational Environmental Satellites – POES – constellations) and from ground–based acquisitions (Super Dual Auroral Radar Network – SuperDARN). Moreover, since this day was characterized by largely varying solar wind and IMF conditions, we discuss about the role played by different solar drivers in the scintillation production.

This paper is organized as follows: section 2 illustrates the method adopted in the study; section 3 discusses the results; section 4 provides discussion of the results; section 5 draws the conclusions.

2. DATA AND METHODS

This paper reports the analysis of GNSS data acquired by GPS Ionospheric Scintillation and TEC Monitor [GISTM, Van Dierendonk et al. 1993] receivers on June 22, 2015. Specifically, we use data from Eureka (EURC), Resolute Bay (RESC) and Ny–Ålesund (NYA0) stations located in the Arctic, and from Concordia (DMC0) and Zhongshan (ZSGN) stations located in Antarctica.

The geographic and corrected geomagnetic coordinates of the receivers are reported in Table 1. Under quiet geomagnetic conditions, EURC, RESC and DMC0 look for most of the day at the polar cap, while NYA0 and ZSGN look at polar cusp/auroral region. This allows both to investigate the ionospheric response in different geomagnetic sector and to perform an interhemispheric comparison.

Each station in Table 1 is equipped with a Novatel GSV4004, able to sample GPS signal phase and amplitude at 50 Hz for each satellite being tracked on L1 (1575.42 MHz). The receiver's firmware provides amplitude and phase scintillation by computing the S_4 [Yeh and Liu, 1982] index every 60 seconds and the σ_Φ [Van Dierendonck et al., 1993] index by considering the standard deviation of detrended carrier phase averaged over intervals of 1, 3, 10, 30 and 60 seconds. It is also able to provide TEC and the rate of TEC change (ROT) values every 15 seconds from combined L1 and L2 (1227.6 MHz) pseudorange and carrier phase measurements.

In order to detect and investigate the ionospheric irregularities induced by the interplanetary medium conditions on June 22, we use σ_ϕ values from 60 seconds average and ROT over 1 minute interval. We avoid reporting here amplitude scintillation, as no meaningful amplitude events were found during the day. The impact on measurements of longer paths through the ionosphere, due to signals from low–elevation satellites, is accounted by using σ_ϕ index verticalization approach proposed by Spogli et al. [2009, 2013]. According to such approach, we project the σ_ϕ index according to the following equation:

$$\sigma_\phi^{vert} = \frac{\sigma_\phi^{slant}}{F(\alpha_{elev})^a} \quad (1)$$

where σ_ϕ is the index directly provided by the receiver at a given elevation angle along the slant path, while $F(\alpha_{elev})$ is the obliquity factor that is defined as (Mannucci et al. 1993):

$$F(\alpha_{elev})^a = \frac{1}{\sqrt{1-\left(\frac{R_e\, cos\, \alpha_{elev}}{R_e + H_{IPP}}\right)^2}} \quad (2)$$

In equation (2), R_e is the Earth's radius and H_{IPP} is the height of the Ionospheric Piercing Point (IPP), which in the present investigation is assumed to be located at 350 km of altitude. According to Rino [1979a, 1979b] and as described by Spogli et al. [2009], the exponent a is equal to 0.5. Although the angular dependence of the σ_ϕ index in equation (1) is valid only under weak scattering condition, we decide to apply the formula for weak scattering to characterize a moderate/strong scintillation scenario as well. In fact, according to Rino [1979a] and as critically discussed by Spogli et al. [2013], the projection to the vertical leads to a σ_ϕ value smaller than the original slant index, so leading to underestimate the corresponding scintillation. As the projection to vertical could underestimate the scintillation level, our method ensures that the detection of high values of σ_ϕ are associated to actual ionospheric effects.

In order to reduce the impact of non–scintillation related tracking errors (such as multipath) a mask of 20° on the elevation angle of the satellites is applied on scintillation data used in this work. In fact, although the 50 Hz sampling frequency adopted by GNSS receivers is useful to investigate transient ionospheric effects, it cannot distinguish the scintillations caused by ionospheric irregularities from multipath due to physical obstacles (buildings, trees, etc.) that may be present in the environment surrounding the receiver antenna.

Location	Station ID	Owner	Latitude	Longitude	CGLat	CGLon
Eureka	EURC	CHAIN	79.99 °N	274.10 °E	87.41 °N	342.32 °E
Resolute Bay	RESC	CHAIN	74.75 °N	265.00 °E	82.45 °N	326.10 °E
Ny- Ålesund 0	NYA0	INGV	78.92 °N	11.98 °E	76.54 °N	108.79 °E
Concordia	DMC0	INGV	75.10 °S	123.35 °E	88.02 °S	225.55 °E
Zhongshan	ZSGN	CAA	69.37 °S	76.37 °E	75.59 °S	102.53 °E

TABLE 1. Locations, identifiers, geographic and geomagnetic coordinates of the used GISTM receivers. CGLat and CGLon stand for "Corrected Geomagnetic" Latitude and Longitude.

As shown by D'Angelo et al. [2015], the choice to apply a mask of 20° on the elevation angle of the satellites is not always effective in eliminating all the multipath effects. Nevertheless, it is difficult to perform a site characterization like the one proposed by D'Angelo et al. [2015] in remote sites such as those selected for the investigation proposed in this work. On the other hand, the polar regions are usually characterized by very few environmental constrains making the choice of 20° elevation mask a good compromise between loss of scintillation data and multipath effects filtering. In addition, to minimize possible mismeasurements of the scintillation indices and ROT following a loss–of–lock event, we take into account only data characterized by lock time on L1 larger than 240 s [Smith et al., 2008]. Lastly, to discriminate between scintillating and not scintillating signals, we choose a threshold of 0.25 radians, which, according to Spogli et al. [2009], identifies scintillations from moderate to strong levels.

In order to infer information about the electron density gradients leading to the observed scintillations and the scale sizes of the ionospheric irregularities involved, we also study the ROT behaviour [Wernik et al., 2004; Zou and Wang, 2009; Alfonsi et al., 2011].

To support the reconstruction of the ionospheric features detected by ROT and scintillation parameters, we combine information coming from GNSS measurements with concurrent supporting information provided by ground–based and space–borne observations. Namely:

- For the local characterization of the ionospheric electron density distribution, we analyse *in-situ* measurements of plasma density in the topside ionosphere provided by Langmuir probes on board Swarm constellation [Friis–Christensen et al., 2006]. The geometry of such constellation allows investigating ionospheric plasma density distribution at different altitudes (460 km for Swarm A and C and 530 km for Swarm B) and different geomagnetic sectors. Furthermore, we compute and analyse the electron density root mean square (*rms*) for each time series related to a polar crossing above |50°| magnetic latitude, for each satellite of the constellation. This can lead to an estimate of the average variability through the polar caps of the electron density at different time of the day.
- In order to have a picture of the high latitude ionosphere dynamics, including its spatial evolution, in connection with the Earth's magnetosphere and the interplanetary perturbation, we leverage on the ionospheric electrostatic potential provided by the Super Dual Auroral Radar Network [SuperDARN, Greenwald et al., 1995]. The isocontours of the potential are reconstructed by means of a statistical model of average convection as a function of the external drivers conditions (above all, the interplanetary magnetic field and the solar wind speed), constrained on the actual data where they are available [e.g. Cousins and Shepherd, 2010]. The convection maps, therefore, can be considered as representative of an average picture of the ionospheric dynamics, and are shown in this study to link the local and global evolution of the polar caps dynamics during the storm. Moreover, we analyse the spectral widths associated with the velocity measurements along the line of sight of the radars. Specifically, we select spectral widths larger than 200 m/s as a threshold to distinguish between different plasma regimes in the ionosphere. Such arbitrary threshold is often found in the literature, for statistically separating ionospheric regions that map on open field lines on the dayside (e.g. the cusp, or the low latitude boundary layer) from regions that map further southward in the oval, on closed field lines. When in the night side, large values of the spectral width are usually associated with regions characterized by a wider dispersion of the plasma velocity distribution, e.g. in presence of vortex structures or plasma shears [e.g. Woodfield et al. 2002; Chisham and Freeman, 2004].

To provide an overall representation of the high–latitude ionospheric irregularities causing the observed phase scintillations, we adopted the same method used in D'Angelo et al., [2018], in which the Altitude Adjusted Corrected GeoMagnetic [AACGM; Baker and Wing, 1989] coordinates (MLat, MLon) and Magnetic Local Time (MLT) are used as the reference frame. For each hemisphere, we provide maps in which SuperDARN observations, Swarm electron density measurements and the projection of the GNSS tracks experiencing scintillation are given simultaneously.

3. RESULTS

Figure 2 shows the time profile of σ_ϕ recorded by EURC and DMC0 (panel a), RESC (panel b), NYA0 and ZSGN (panel c) on June 22, 2015. Panels a and c report the comparison between Northern and Southern GNSS observations recorded at ground by receivers, which look, under quiet geomagnetic conditions, roughly conjugated ionospheric regions. The black horizontal lines indicate the 0.25 radians σ_ϕ threshold. The dashed vertical lines, instead, mark the arrival at the Earth's magnetopause of the first (red) and the second interplanetary

shock (green) on June 22. Different colours refers to different satellites in view.

It is worth noting that all the scintillation events were recorded after the arrival of both the interplanetary shocks and appear longer lasting in the Southern Hemisphere. In addition, the EURC receiver did not record significant scintillation events during the day, while the RESC receiver, although located at few magnetic latitude degrees southward than EURC (Table 1), recorded three scintillation events at ~20:45 UT, ~22:00 UT and ~23:30 UT with mean intensities of ~0.50 radians, of ~0.60 radians and of ~0.42 radians, respectively. The DMC0 receiver recorded two scintillation series between ~08:00 UT and 10:00 UT and between ~19:00 UT and 23:00 UT, with mean intensities of ~0.45 radians and of ~0.57 radians, respectively. The NYA0 and ZSGN σ_ϕ time profiles show similar behaviours during the entire day, even if the receiver at ZSGN recorded more intense scintillation events than NYA0. An exception occurred between ~20:00 UT and 21:00 UT, when NYA0 recorded a scintillation of ~0.99 radians.

Figure 3 shows the ROT time profiles for the same stations and in the same time interval as above. Also in this case, the dashed vertical lines mark the arrival at the magnetopause of the first (red) and second (green) interplanetary shock and different colours refer to different satellites in view. The most intense and sudden ROT excursions were recorded after the arrival of the two interplanetary shocks, as visible in all panels of Figure 3. Such excursions appear longer lasting and more intense in the Southern Hemisphere and after the arrival of the second interplanetary shock. They also occur mainly in correspondence with the scintillation events in Figure 2.

Figure 4 shows polar view maps, covering |50°|–|90°| MLat and 00:00–24:00 MLT for the Northern (top) and the Southern (bottom) Hemispheres. Each map displays an overview of the ionospheric convection patterns (ionospheric electrostatic potential reconstructed by SuperDARN, red/blue isocontours mean positive/negative values of the potential) in the time interval 07:00–10:00 UT, corresponding to the first significant scintillation peak recorded on June 22 (Figure 2). Furthermore, each map reports the intensity profile of electron density (black line, whose thickness expresses the electron density variation) recorded by Swarm A (SWA) or B (SWB). In addition, each map reports the projection of ionospheric scintillation (colour dots), simultaneously recorded by Eureka, Resolute Bay and Ny–Ålesund stations in the Northern Hemisphere (top panels) and by Concordia and Zhongshan stations in the Southern Hemisphere (bottom panels). In each map, we also report all SuperDARN observations of spectral widths: we highlight spectral widths values greater than 200 m/s by means of blue squares, while values lower than 200 m/s are represented by black squares. The SuperDARN data were collected along the two minutes after the time shown at the top of each map.

Figure 4 confirms that scintillation originated in the cusp region of both hemispheres. Moreover, high spectral width values (blue squares) occur, in the Northern Hemisphere, mainly in the early pre–dawn sector of the auroral oval (around 3 MLT, panels a and e), while, in the Southern Hemisphere, they occur mainly in the cusp and between the two convection cells (panels b and d). The overall convection patterns, both in the Northern and in the Southern Hemispheres, are coherent with a scenario dominated by $B_{z,\,IMF}$ predominantly negative, with convection cells tilted towards dawn by the effect of a mainly positive $B_{y,\,IMF}$ (panels c and d in Figure 1).

Figure 5 shows the polar maps for the Northern (top) and the Southern (bottom) Hemispheres in the time interval 19:00 to 23:00 UT (i.e. when the second significant scintillation peak occurs, see Figure 2). It is worth noticing that scintillations mainly occur in the Southern Hemisphere and appear between the two convection cells. Several authors [see, e.g., De Franceschi et al 2008; Mitchell et al 2005; Moen et al. 2013] identified the region between the two convection cells as the best candidate to host the ionospheric irregularities causing scintillations. In addition, scintillations occur close to the region in which Swarm observes clear increases of electron density (evidenced by an enhanced thickness of the Swarm track, Figure 5 bottom panels). Concerning the spectral width, in the Northern Hemisphere, the higher values are mainly concentrated in the cusp and in the early morning sector of the auroral oval. In the Southern Hemisphere, they are almost missing. The comparison between Northern and Southern maps in Figure 5 shows that the low/null number of spectral width observations above threshold (blue squares) recorded in the Southern Hemisphere could be associated with ionospheric absorption rather than with quiet ionospheric conditions. In fact, in the Southern Hemisphere also the number of spectral width observation < 200 m/s is low (black squares). The overall convection symmetry is very similar with respect to the earlier interval considered above, with $B_{z,\,IMF}$ fluctuating around zero between 19:30 and 21:00 UT, supported by a strongly positive $B_{y,\,IMF}$ (see Figure 1, panels c, d). After about 21 UT, $B_{z,\,IMF}$ reaches a more stable trend, keeping positive values: this is consistent with the shrinking of the polar cap, particularly evident in the Northern Hemisphere (Figure 5, panels p and r). Southern Hemisphere seems to keep the usual symmetry of the

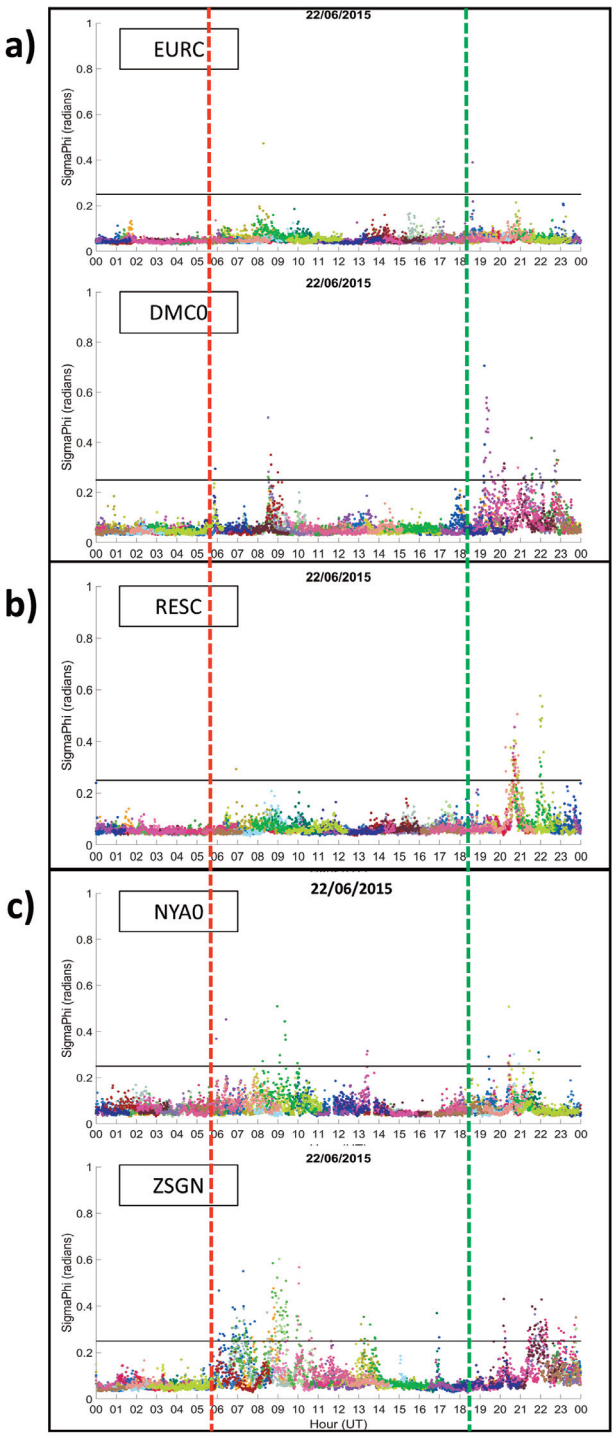

FIGURE 2. Time profiles of σ_Φ recorded by EURC and DMC0 (a), RESC (b), NYA0 and ZSGN (c) receivers during June 22, 2015. Different colours refers to different satellites in view. The dashed vertical lines mark the arrival at the magnetopause of the first (red) and the second interplanetary shock (green). The black horizontal lines characterize the 0.25 radians threshold, which defines the transition from weak (below the line) to strong (above the line) phase scintillation levels.

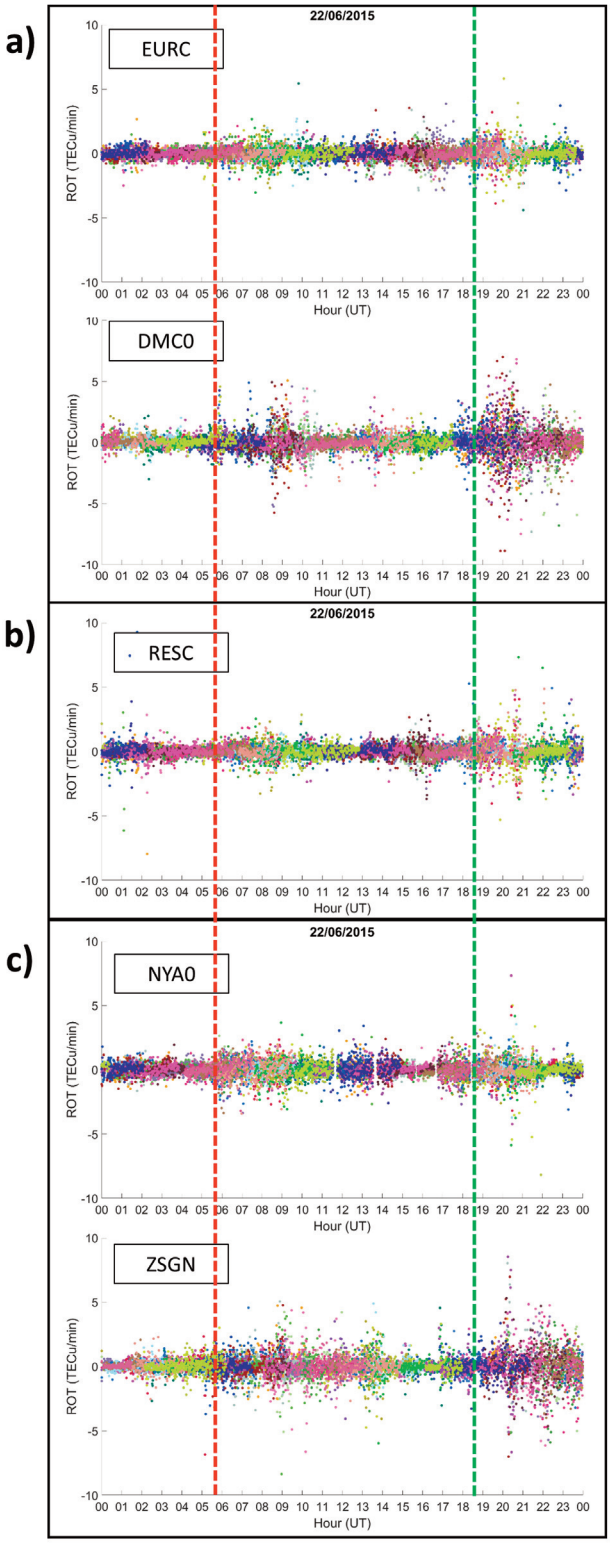

FIGURE 3. Time profiles of ROT, recorded by EURC and DMC0 (a), RESC (b), NYA0 and ZSGN (c) receivers, during June 22, 2015. Different colours refer to different satellites in view. The dashed vertical lines mark the arrival at the magnetopause of the first (red) and the second interplanetary shock (green).

convection patterns, even after 21:00 UT, but this could be an artefact of the convection model, being the actual SuperDARN measurements very sparse in the Southern Hemisphere during this interval.

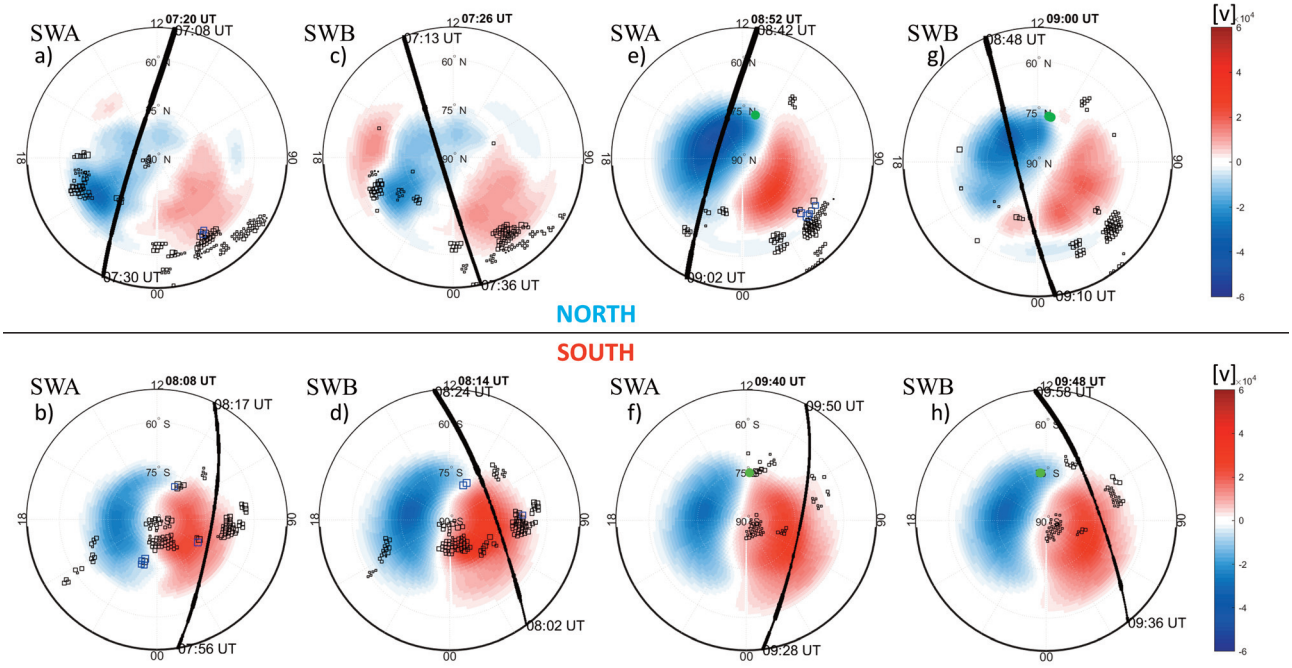

FIGURE 4. Polar view maps in AACGM coordinates for the Northern (top) and sSuthern Hemispheres (bottom) between 07:00–10:00 UT of 2017 June 22. Each map shows: the isocontours of the ionospheric potential (red=positive, blue=negative potential), recorded in the two minutes following the time shown at the top of each map; SuperDARN measurements of spectral widths lower than 200 m/s (black squares) and higher than 200 m/s (blue squares); the electron density (black line) recorded along the orbits of Swarm A (SWA) and B (SWB) satellites; phase scintillations greater than 0.25 radians (coloured dots) recorded simultaneously along the Swarm tracks. In each map, which covers 00:00–24:00 MLT and |50°|–|90°| MLat, the magnetic noon/midnight is at the top/bottom.

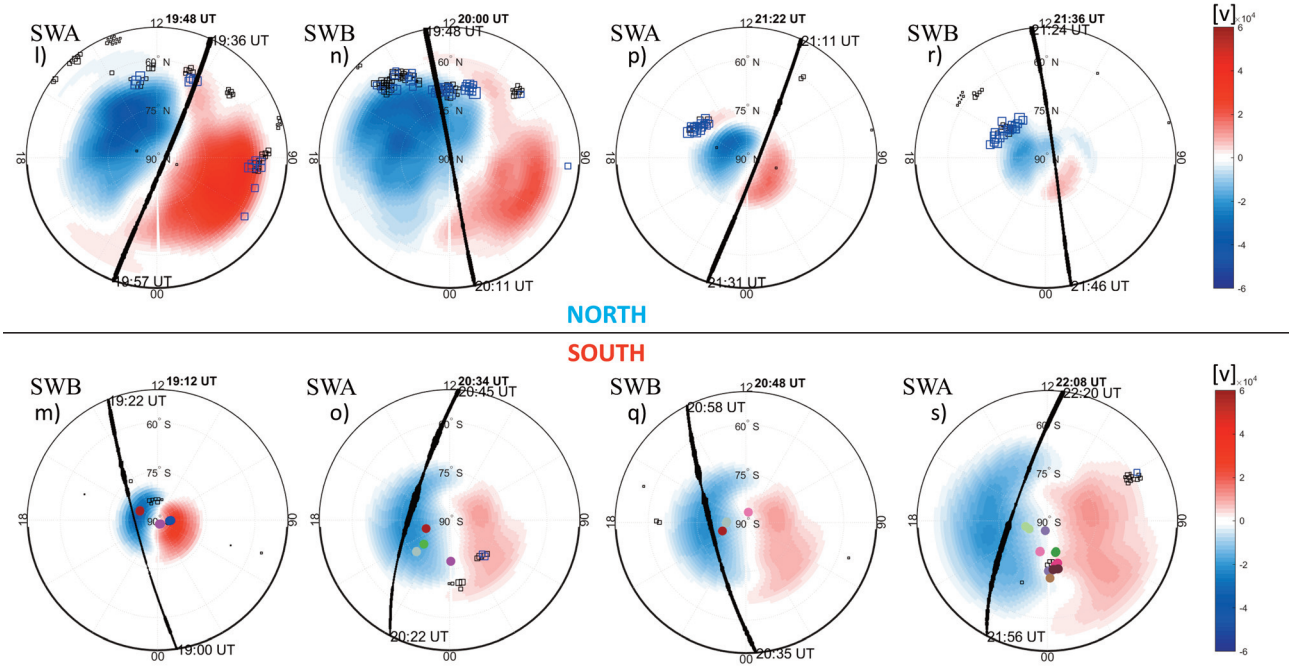

FIGURE 5. Polar view maps in AACGM coordinates for the Northern (top) and Southern Hemispheres (bottom) between 19:00–23:00 UT of 2017 June 22. Each map shows: the isocontours of ionospheric potential (red=positive, blue=negative potential), recorded in the two minutes following the time shown at the top of each map; SuperDARN measurements of spectral widths lower than 200 m/s (black squares) and higher than 200 m/s (blue squares); the electron density (black line) recorded along the traces of Swarm A (SWA) and B (SWB) satellites; phase scintillations greater than 0.25 radians (coloured dots) recorded simultaneously along the Swarm tracks. In each map, which covers 00:00–24:00 MLT and |50°|–|90°| MLat, the magnetic noon/midnight is at the top/bottom.

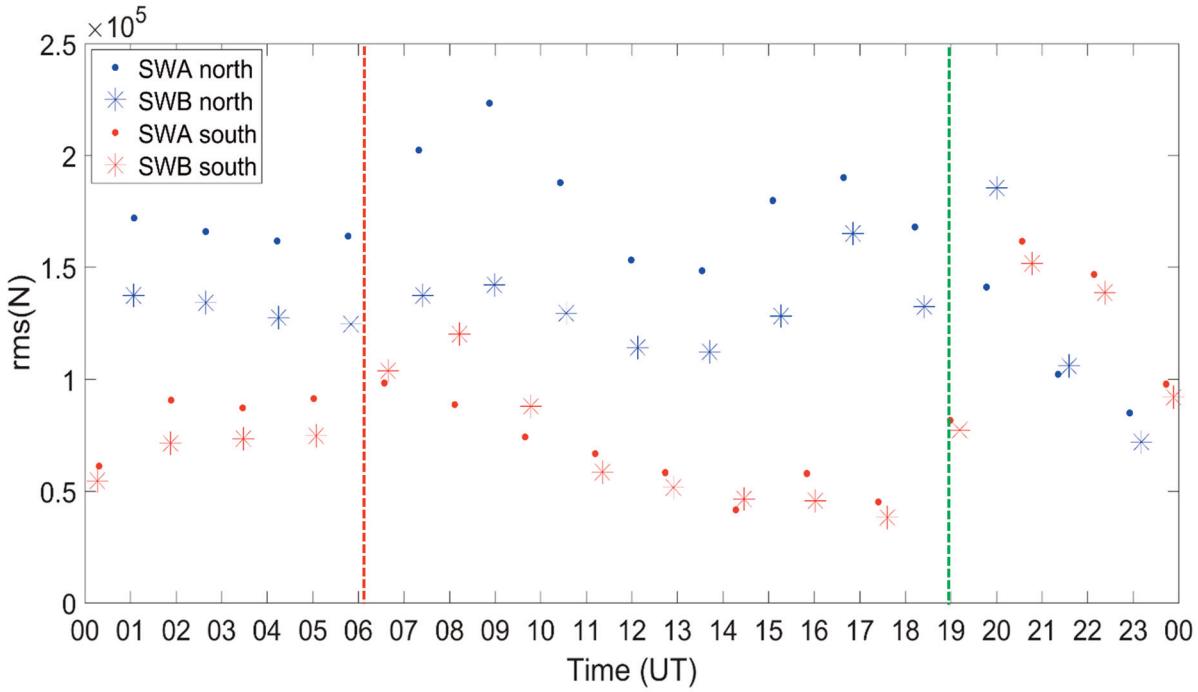

FIGURE 6. Electron density root mean square (*rms*) measured by Swarm A (circles) and Swarm B (stars) during June 22, 2015. Blue series refers to measurements in the Northern Hemisphere, while red series refers to measurements in the Southern Hemisphere. The magnetic latitude ranges between |50°| and |90°|. Dashed vertical lines mark the arrival at the magnetopause of the first (red) and second (green) interplanetary shock.

Figure 6 shows the time profile of the *rms* of the ionospheric *in-situ* electron density measured by Swarm A (SWA, circles) and Swarm B (SWB, stars) during June 22, in both polar regions within 50° of magnetic latitude. Dashed vertical lines mark the arrival at the magnetopause of the first (red) and second (green) interplanetary shock. Until ~18:30 UT, the *rms* in the Southern Hemisphere (red) is three times smaller than in the Northern Hemisphere (blue). At the same time, in the Southern Hemisphere the SWA *rms* (red circles) is roughly comparable with SWB *rms* (red stars). Conversely, in the Northern Hemisphere, *rms* appears greater (blue circles) for SWA than for SWB (blue stars). After the shocks arrivals at the Earth's magnetopause (red and green dashed lines), the two satellites observed a higher electron density *rms* in both hemispheres. After the arrival of the second shock (green line), the *rms* in Southern Hemisphere (red) becomes greater than in the Northern Hemisphere (blue). In addition, the *rms* of SWA (blue circles) becomes comparable with those of SWB (blue stars), in the Northern Hemisphere.

4. DISCUSSION

Although the June 2015 geomagnetic storm was one of the most intense storms of the 24th solar cycle [Astafyeva et al., 2017; Piersanti et al., 2017], the observed scintillation was not as intense (Figure 2) as during the 2015 St. Patrick's day storm [D'Angelo et al., 2018]. This unexpected behaviour might be associated with two possible reasons. The first is the peculiar conditions of the $B_{z,\,IMF}$ recorded on June 22, 2015. In fact, $B_{z,\,IMF}$ first showed fluctuations around zero until the arrival of the second shock, and then a large–brief negative excursion (see panel d in Figure 1). Such condition is less effective in producing moderate/intense scintillation events than a negative, long lasting $B_{z,\,IMF}$ condition. The second reason is the insufficient geomagnetic sectors coverage of the GNSS receivers used in this analysis. In fact, according to Cherniak and Zakharenkova, [2017], a large number of plasma density fluctuations just occurred in both auroral regions that are not in the field of view of our GNSS network.

In order to verify how the observed scintillation is related to particle precipitation, in Figure 7 we show the electron and proton total atmospheric integral energy flux as a function of the magnetic latitude from POES [Evans and Greer, 2004] constellation observations, integrated at 120 km on June 22, 2015. In particular, starting from the electron and proton total atmospheric integral energy fluxes we calculate the total particle–precipitation fluxes in two time intervals: the first, between the two shocks arrivals (Figure 7a), the second

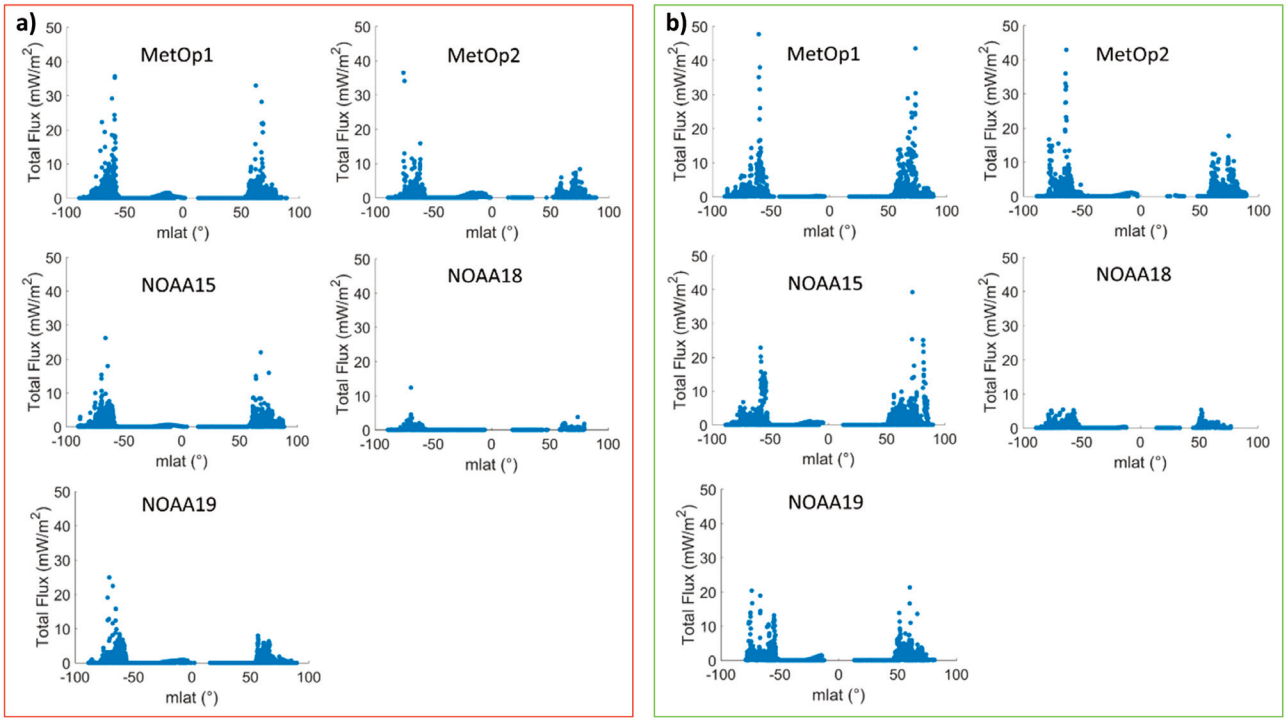

FIGURE 7. Electron and Proton total atmospheric integral energy flux at 120 km as a function of the magnetic latitude, measured by the TED (Total Energy Detector) on board of MetOp1, MetOp2, NOAA15, NOAA18, NOAA19 satellites of the POES constellation, during 2015–06–22. Panel a) reports fluxes measured in the time interval between the arrival of the first and second shock. Panel b) reports fluxes measured in the time interval from the arrival of the second shock and the end of the day.

between the arrival of the second shock and the end of the day (Figure 7b). After the arrival of the first shock (panel a), the most intense particle precipitation occurs in the Southern Hemisphere. Correspondingly, DMC0 and ZSGN show longer lasting phase scintillations (Figure 2) with respect to the Northern receivers. Figure 7b shows that at the arrival of the second shock a quite symmetrical particle precipitation occurs in both hemispheres. At the same time, Figure 2 shows scintillations in all the investigated ionospheric regions of both hemispheres, with the exception of the Northern polar cap. It is important to note that the absence of amplitude scintillations allows correlating the phase scintillation with refractive effects [Yeh and Liu, 1982; Kintner et al., 2007] that may be associated with the plasma dynamics caused by the particles precipitation. In fact, the latter determines an increase in the ionospheric electrojets that may inhibit the formation of irregularities near the first Fresnel radius.

Furthermore, Figure 2 shows that our network recorded during the day phase scintillations characterized by almost the same intensities in both hemispheres. Such behaviour can be associated with the geometry of the shocks hitting the Earth's magnetopause. In fact, the estimated shocks normal orientations, evaluated by applying the Rankine Hugoniot's conditions [see e.g. Tidman and Krall, 1971] on solar wind data, (Table 2), lie almost in the ecliptic plane and hit the magnetopause almost at noon [Villante et. al, 2008; Alberti et al. 2016; Piersanti et al. 2016]. Actually, the *rms* variations (Figure 6) show a similar behaviour in both hemispheres, despite the offset between Northern and Southern *rms*. Such offset can be associated with seasonal effects. In fact, the different ionospheric background, in terms of ionization, produces, in this case event, a larger *rms* in the summer hemisphere (the Northern one). The consequence of a more Northern hitting of the first shock onto the magnetopause (Table 2a) coupled with the $B_{z,\,IMF}$ oscillations around zero, can be responsible of the larger *rms* of SWA's electron density in the Northern Hemisphere (blue circles in Figure 6). In addition, the consequence of a more Southern hitting of the second shock onto the magnetopause (Table 2b) coupled with the huge negative $B_{z,\,IMF}$ values, can be responsible of the enhancement of the Southern *rms*, which becomes comparable to the Northern one.

Lastly, following the analysis proposed by Alfonsi et al., [2011] and Wernik et al., [2004], we compare the ROT time profiles (Figure 3) to the σ_ϕ variations (Figure 2), recorded by all GNSS receivers. Such comparison with the absence of amplitude scintillation events allows deducing that irregularities of largely varying

a) First shock parameters	
IP shock's normal latitude (GSE):	$\theta = 150.4°$
IP shock's normal longitude (GSE):	$\phi = 112.2°$
IP shock's speed:	$V_{IP} = 450\ km/s$
IP shock's impact point at magnetopause:	$X_{imp_{GSE}} = 10.7\ R_E$
	$Y_{imp_{GSE}} = 1.8\ R_E$

b) Second shock parameters	
IP shock's normal latitude (GSE):	$\theta = 173.6°$
IP shock's normal longitude (GSE):	$\phi = 99.8°$
IP shock's speed:	$V_{IP} = 450\ km/s$
IP shock's impact point at magnetopause:	$X_{imp_{GSE}} = 8.9\ R_E$
	$Y_{imp_{GSE}} = 6.9\ R_E$

TABLE 2. Interplanetary shocks parameters. Table a (red) reports the resulting parameters of the first shock, while table b (green) reports the resulting parameters of the second shock.

scale–sizes occupied the investigated regions although their dimensions were far from the first Fresnel radius. This result agrees either with Cherniak and Zakharenkova [2017], who showed the presence of a large number of plasma density fluctuations over both hemispheres during the day, and with Swarm electron density observations, which showed the presence of electron density enhancements in the both polar regions (Figure 4, Figure 5). Moreover, the electron density variations induced by the storm drivers, confirmed also by the Swarm *rms* electron density variations (Figure 6), can be related to the concurring manifestation of scintillations (Figure 2), confirming the direct link between scintillation and abrupt changes in plasma distribution.

5. CONCLUSIONS

This paper investigates how ionospheric irregularities, triggered by the June 2015 storm, lead to phase scintillation events in the high–latitude ionosphere of both hemispheres. To investigate the origin and the evolution of the ionospheric irregularities causing scintillations, we combine information from scintillation parameters and ROT (derived from GNSS receivers) with measurements acquired by SuperDARN, Swarm and POES constellations.

This study highlights how a detailed reconstruction of the ionospheric scenario in which irregularities causing scintillation form and move can be achieved through a multi–observation approach. Such approach, indeed, allows deducing that scintillations were due to the presence of fast–moving electron density gradients, of several scale–sizes that are far from the first Fresnel radius, originated by particle precipitation associated with the arrival, at the Earth's magnetopause, of two interplanetary shocks. Nevertheless, although the June storm was the second largest storm of the 24th solar cycle, it did not produce severe scintillation events in the investigated regions. We attributed such effect to the peculiar conditions of the $B_{z,\ IMF}$ that showed numerous and fast oscillations for most of the June 22, which are less effective in producing moderate/intense scintillation events than during period characterized by long lasting negative values of $B_{z,\ IMF}$.

Additionally, such approach provides insights about the link between the GPS phase scintillation and the ionospheric plasma distribution. In fact, the comparison between σ_ϕ and ROT variations and the *rms* of Swarm electron density measurements suggests that the ionospheric regions, characterized by strongly variables electron density, are most likely to give rise to phase scintillation.

Our results show that the combined use of data from *in-situ* and ground–based sensors allows a detailed characterization of ionospheric dynamics during a geomagnetic storm. Being the ionospheric scintillation a complex effect and hard to predict, the study of the ionosphere at different heights and with different sampling frequencies can provide information useful to better characterize the scintillation triggers in the high latitude ionosphere. In the Space Weather context, this can open the door to new approaches to realize scintillations prediction tools, especially in terms of identification of the geomagnetic sectors most likely to be affected by scintillations.

ACKNOWLEDGEMENTS. The authors thank PNRA (Programma Nazionale di Ricerche in Antartide) for supporting the upper atmosphere observations at Concordia Station (Antarctica), and CNR (Consiglio Nazionale delle Ricerche) for supporting the upper atmosphere observations at Dirigibile Italia Station at Ny Alesund (Svalbard). The authors thank Dr. Giorgiana De Franceschi, Dr. Vincenzo Romano and Dr. Ingrid Hunstad for management of the INGV (Istituto Nazionale di Geofisica e Vulcanologia) stations. The authors acknowledge the use of SuperDARN data. SuperDARN is a collection of radars funded by national scientific funding agencies of Australia, Canada, China, France, Italy, Japan, Norway, South Africa, United Kingdom and the United States of America. Eureka and Resolute Bay GNSS data are provided by Canadian High Arctic Ionospheric Network (CHAIN, http://chain.physics.unb.ca). Infrastructure funding for CHAIN was provided by the Canada Foundation for Innovation and the New Brunswick Innovation Foundation. CHAIN and CGSM operation is conducted in collaboration with the Canadian Space Agency (CSA). Zhongshan GNSS data are provided by Beijing National Observatory of Space Environment IGGCAS through the Data Center for Geophysics, National Earth System Science Data Sharing Infrastructure. The solar wind plasma and magnetic field data of WIND, as well as the POES data, were obtained from the NASA's cdaweb site (http://cdaweb.gsfc.nasa.gov/istp_public/). Swarm data are provided by the European Space Agency upon registration (https://earth.esa.int/web/guest/swarm/data-access/). We kindly thank Dr. Stephan Buchert from IRFU, Sweden, for providing the Swarm Langmuir Probe Extended Dataset. This research work is supported by the Italian MIUR-PRIN grant 2012P2HRCR on *The active Sun and its effects on Space and Earth climate*.

REFERENCES

Alberti, T., M. Piersanti, A. Vecchio, P. De Michelis, F. Lepreti, V. Carbone, and L. Primavera (2016). Identification of the different magnetic field contributions during a geomagnetic storm in magnetospheric and ground observations. Ann. Geophysicae, doi: 10.5194/angeo–34–1069–2016.

Alfonsi, L., L. Spogli, G. De Franceschi, V. Romano, M. Aquino, A. Dodson and C. N. Mitchell (2011). Bipolar climatology of GPS ionospheric scintillation at solar minimum. Radio Science, 46(3), doi: 10.1029/2010RS004571.

Astafyeva, E., I. Zakharenkova, and P. Alken, (2016). Prompt penetration electric fields and the extreme topside ionospheric response to the June 22–23, 2015 geomagnetic storm as seen by the Swarm constellation. Earth, Planets and Space, 68(1), 152.

Astafyeva, E., I. Zakharenkova, J. D. Huba, E. Doornbos, and J. van den Ijssel (2017). Global Ionospheric and Thermospheric Effects of the June 2015 Geomagnetic Disturbances: Multi Instrumental Observations and Modeling. Journal of Geophysical Research: Space Physics, 122(11).

Baker, K. B. and S. Wing, (1989). A new magnetic coordinate system for conjugate studies at high latitudes. J. Geophys. Res., 94, 9139–9143, 1989.

Cherniak, I., and I. Zakharenkova (2017). New advantages of the combined GPS and GLONASS observations for high–latitude ionospheric irregularities monitoring: case study of June 2015 geomagnetic storm. Earth, Planets and Space, 69(1), 66.

Chisham, G. and M. P. Freeman (2004). An investigation of latitudinal transition in the SuperDARN Doppler spectral width parameter at different magnetic local times. Annales Geophysicae, 22, 1187 – 1202.

Cousins, E. D. P. and S. G. Shepherd (2010). A dynamical model of high latitude convection derived from SuperDARN plasma drift measurements. J. Geophys. Res., Space 115. doi: 10.1029/2010JA016017.

D'Angelo, G., L. Spogli, C. Cesaroni, V. Sgrigna, L. Alfonsi and M. H. O. Aquino, (2015). GNSS data filtering optimization for ionospheric observation. Advances in Space Research, 56(11), 2552–2562.

D'Angelo, G., M. Piersanti, L. Alfonsi, L. Spogli, L.B.N Clausen, I. Coco, G. Li, N. Baiqi (2018). The response of high latitude ionosphere to the 2015 St. Patrick's Day storm from in situ and ground based observations. Advances in Space Research, 62(3), 638–650.

De Franceschi, G., L. Alfonsi, and V. Romano (2006). ISACCO: an Italian project to monitor the high latitudes ionosphere by means of GPS receivers. GPS Solutions, 10(4), 263–267.

De Franceschi G., L. Alfonsi, V. Romano, M. Aquino, A. Dodson, C.N. Mitchell, P. Spencer and A. W. Wernik (2008). Dynamics of high–latitude patches and associated small–scale irregularities during the October and November 2003 storms. Journal of Atmospheric and Solar–Terrestrial Physics, 70(6), 879–888.

Evans, D., and M. Greer (2004). Polar Orbiting Environmental Satellite Space Environment Monitor–2: Instrument Descriptions and Archive Data Documentation. Technical Memorandum 93, NOAA, Boulder, Colorado OAR SEC 93, Version 1.4. January.

Friis–Christensen, E., H. Lühr and G. Hulot (2006). Swarm: A constellation to study the Earth's magnetic field. Earth, Planets and Space, Vol. 58, p. 351–358, doi: 10.1186/BF03351933

Greenwald, R. A., K. B. Baker, J. R. Dudeney, M. Pinnock, T. B. Jones, E. C. Thomas, J. P. Villain, J. C. Cerisier, C. Senior, C. Hanuise, R. D. Hunsucker, G. Sofko, J. Koehler, E. Nielsen, R. Pellinen, A. D. M. Walker, N. Sato, and H. Yamagishi (1995). Darn/superdarn. Space Science Reviews, 71(1–4), 761–796.

Jayachandran, P. T., R. B. Langley, J. W. MacDougall, S. C. Mushini, D. Pokhotelov, A. M. Hamza, I. R. Mann, D. K. Milling, Z. C. Kale, R. Chadwick, T. Kelly, D. W. Danskin, and C. S. Carrano, (2009). Canadian high arctic ionospheric network (CHAIN). Radio Science, 44(1), doi: 10.1029/2008RS004046.

Kintner, P. M., B. M. Ledvina and E. R. De Paula (2007). GPS and ionospheric scintillations. Space weather, 5(9).

Liu, Y. D., H. Hu, R. Wang, Z. Yang, B. Zhu, Y. A. Liu, J. G. Luhmann, and J. D. Richardson (2015). Plasma and magnetic field characteristics of solar coronal mass ejections in relation to geomagnetic storm intensity and variability. The Astrophysical Journal Letters, 809(2), L34.

Mannucci, A. J., Wilson, B. D. and C. D. Edwards (1993). A new method for monitoring the Earth ionosphere total electron content using the GPS global network. Paper presented at ION GPS 93, Inst. of Navig., Salt Lake City, Utah.

Mansilla, G. A. (2018). Ionospheric Response to the Magnetic Storm of 22 June 2015. Pure and Applied Geophysics, 175(3), 1139–1153.

Mitchell, C.N., L. Alfonsi, G. De Franceschi, M. Lester, V. Romano and A.W. Wernik (2005). GPS TEC and scintillation measurements from the polar ionosphere during the October 2003 storm. Geophysical Research Letters 32, L12S03.

Moen, J., K. Oksavik, L. Alfonsi, Y. Daabakk, V. Romano and L. Spogli (2013). Space weather challenges of the polar cap ionosphere. J. Space Weather Space Clim., 3, A02, doi:10.1051/swsc/2013025.

Piersanti, M. and U. Villante, (2016). On the discrimination between magnetospheric and ionospheric contributions on the ground manifestation of sudden impulses. J. Geophys. Res., Space 121(7), 6674. doi: 10.1002/2015JA021666.

Piersanti, M., T. Alberti, A. Bemporad, F. Berrilli, R. Bruno, V. Capparelli and A. Del Corpo (2017). Comprehensive Analysis of the Geoeffective Solar Event of 21 June 2015: Effects on the Magnetosphere, Plasmasphere, and Ionosphere Systems. Solar Physics, 292(11), 169.

Prikryl, P., L. Spogli, P. T. Jayachandran, J. Kinrade, C. N. Mitchell, B. Ning and B. D. L.Opperman (2011). Interhemispheric comparison of GPS phase scintillation at high latitudes during the magnetic–cloud–induced geomagnetic storm of 5–7 April 2010. In Annales Geophysicae, 29, 2287–2304.

Prikryl, P., Yongliang Zhang, Yusuke Ebihara, Reza Ghoddousi–Fard, Periyadan T. Jayachandran, Joe Kinrade, Cathryn N. Mitchell, Allan T. Weatherwax, Gary Bust, Pierre J. Cilliers, Luca Spogli, Lucilla Alfonsi, Vincenzo Romano, Baiqi Ning, Guozhu Li, Martin J. Jarvis, Donald W. Danskin, Emma Spanswick, Eric Donovan, Mike Terkildsen (2013). An interhemispheric comparison of GPS phase scintillation with auroral emission observed at South Pole and from DMSP satellite. Annals of Geophysics, 56(2).

Prikryl, P., R. Ghoddousi–Fard, L. Spogli, C. N. Mitchell, G. Li, B. Ning, P. J. Cilliers, V. Sreeja, M. Aquino, M. Terkildsen, P. T. Jayachandran, Y. Jiao, Y. T. Morton, J. M. Ruohoniemi, E. G. Thomas, Y. Zhang, A. T. Weatherwax, L. Alfonsi, G. De Franceschi, and V. Romano (2015). GPS phase scintillation at high latitudes during geomagnetic storms of 7–17 March 2012–Part 2: Interhemispheric comparison. Annales Geophysicae, 33, 657–670.

Rino, C. L. (1979a). A power law phase screen model for ionospheric scintillation: 1. Weak scatter. Radio Science, 14(6), 1135–1145.

Rino, C. L. (1979b). A power law phase screen model for ionospheric scintillation: 2. Strong scatter. Radio Science, 14(6), 1147–1155.

Smith, A. M., C. N. Mitchell, R. J. Watson, R. W. Meggs, P. M. Kintner, K. Kauristie and F. Honary, (2008). GPS scintillation in the high arctic associated with an auroral arc. Space Weather, 6(3).

Spogli, L., L. Alfonsi, G. De Franceschi, V. Romano, M. H. O. Aquino, and A. Dodson (2009). Climatology of GPS ionospheric scintillations over high and mid latitude European regions. Annales Geophysicae, 27, 3429–3437, doi: 10.5194/angeo–27–3429–2009.

Spogli, L., L. Alfonsi, V. Romano, G. De Franceschi, G. M. J. Francisco, M. H. Shimabukuro, and Aquino, M. (2013). Assessing the GNSS scintillation climate over Brazil under increasing solar activity. Journal of Atmospheric and Solar–Terrestrial Physics, 105, 199–206, doi:

10.1016/j.jastp.2013.10.003.

Tidman, D. A. and N. A. Krall (1971). Shock waves in collisionless plasmas. New York: Wiley–Inter–science, 99–112.

Van Dierendonck, A. J., J. Klobuchar, and Q. Hua, (1993). Ionospheric scintillation monitoring using commercial single frequency C/A code receivers. In proceedings of ION GPS, 93, 1333–1342.

Villante, U., M. and Piersanti, M. (2008). An analysis of sudden impulses at geosynchronous orbit. J. Geophys. Res., 113, A08213, doi:10.1029/2008JA013028.

Wernik, A. W., L. Alfonsi and M. Materassi (2004). Ionospheric irregularities, scintillation and its ef–fect on systems. Acta geophysica polonica, 52(2), 237–249.

Woodfield, E. E., K. Hosokawa, S. E. Milan, N. Sato and M. Lester (2002). An interhemispheric, statistical study of nightside spectral width distributions from coherent HF scatter radars. Annales Geo–physicae, 20(12), 1921–1934.

Yeh, K. C., and C. H. Liu (1982). Radio wave scintilla–tions in the ionosphere. Proceedings of the IE, 70(4), 324–360.

Zou, Y., and D. Wang, D. (2009). A study of GPS ionos–pheric scintillations observed at Guilin. Journal of Atmospheric and Solar–Terrestrial Physics, 71(17), 1948–1958.

*CORRESPONDING AUTHOR: Giulia D'ANGELO,
Dipartimento di Matematica e Fisica,
Università degli Studi "Roma Tre", Rome, Italy
email: giulia.dangelo@uniroma3.it